Non-ENSO Precursors for Northwestern Pacific Summer Monsoon Variability with Implications for Predictability

PENGCHENG ZHANG,[a] SHANG-PING XIE,[a] YU KOSAKA,[b] AND NICHOLAS J. LUTSKO[a]

[a] Scripps Institution of Oceanography, University of California San Diego, La Jolla, California
[b] Research Center for Advanced Science and Technology, The University of Tokyo, Tokyo, Japan

(Manuscript received 23 March 2023, in final form 10 October 2023, accepted 18 October 2023)

ABSTRACT: The influence of El Niño–Southern Oscillation (ENSO) in the Asian monsoon region can persist through the post-ENSO summer, after the sea surface temperature (SST) anomalies in the tropical Pacific have dissipated. The long persistence of coherent post-ENSO anomalies is caused by a positive feedback due to interbasin ocean–atmospheric coupling, known as the Indo-western Pacific Ocean capacitor (IPOC) effect, although the feedback mechanism itself does not necessarily rely on the antecedence of ENSO events, suggesting the potential for substantial internal variability independent of ENSO. To investigate the respective role of ENSO forcing and non-ENSO internal variability, we conduct ensemble "forecast" experiments with a full-physics, globally coupled atmosphere–ocean model initialized from a multidecadal tropical Pacific pacemaker simulation. The leading mode of internal variability as represented by the forecast-ensemble spread resembles the post-ENSO IPOC, despite the absence of antecedent ENSO forcing by design. The persistent atmospheric and oceanic anomalies in the leading mode highlight the positive feedback mechanism in the internal variability. The large sample size afforded by the ensemble spread allows us to identify robust non-ENSO precursors of summer IPOC variability, including a cool SST patch over the tropical northwestern Pacific, a warming patch in the tropical North Atlantic, and downwelling oceanic Rossby waves in the tropical Indian Ocean south of the equator. The pathways by which the precursors develop into the summer IPOC mode and the implications for improved predictability are discussed.

KEYWORDS: Atmosphere-ocean interaction; Monsoons; Interannual variability; Internal variability

1. Introduction

The Asian monsoon system dominates a large swath of the Asian continent from India through eastern China to Japan, home to roughly half of the global population. In these regions, much of the annual precipitation happens in the summer monsoon season, and abnormal monsoons may lead to floods or droughts. Therefore, understanding the variability of the Asian monsoon is of great interest. The summer Asian monsoon is affected by a recurrent low-level anomalous anticyclone (AAC) in the northwestern Pacific (NWP) (Wang et al. 2003; Xie 2022). The center of the AAC resides over the Philippine Sea, but the anomalous easterly winds on its southern flank extend through the South China Sea (SCS) and the Bay of Bengal (BoB) to the Arabian Sea, regulating moisture transport and wind convergence/divergence in the Indo-Pacific region (Xie et al. 2016).

The AAC has considerable interannual variability, which has been linked to El Niño–Southern Oscillation (ENSO) (e.g., Wang et al. 2003). Specifically, the summer AAC is significantly correlated with the ENSO state of the previous boreal winter, rather than that of the concurrent summer (Wang et al. 2018). This time lag is explained by the Indo-western Pacific Ocean capacitor (IPOC) effect (Xie et al. 2016): El Niño events peak in winter, which warms sea surface temperatures (SSTs) in the tropical Indian Ocean (TIO) by anomalous surface heat flux adjustments (Alexander et al. 2002; Du et al. 2009) and by inducing downwelling ocean Rossby waves in the southern IO that propagate slowly westward (Masumoto and Meyers 1998). The slowly propagating ocean Rossby waves and the accumulation of anomalous surface heat flux prolong the TIO warming peak until the following spring (Xie et al. 2002). In summer, the IO warming is coupled with the AAC when the background monsoonal wind over the northern Indian Ocean (NIO) becomes southwesterly: the anomalous easterlies on the southern flank of the AAC extend over the NIO and warm the region by weakening the background monsoonal wind (Du et al. 2009; Kosaka et al. 2013; Xie et al. 2016; Zhu et al. 2022), while positive IO SST anomalies excite the AAC (Terao and Kubota 2005; Yang et al. 2007; Li et al. 2008) via a Kelvin wave–induced Ekman divergence mechanism. This interbasin positive feedback is crucial for sustaining the summer AAC, and the lagged response is analogous to a capacitor, charging during winter El Niño events and discharging in the ensuing summer (Xie et al. 2009; Kosaka et al. 2013; Xie et al. 2016). In addition, the anomalous easterlies on the southeastern flank of the AAC reinforce the background trade winds east of the monsoon trough and cool the SSTs, further strengthening the AAC via a Rossby wave response (Wu et al. 2010; Wang et al. 2013).

Although the preceding ENSO explains much of the summer AAC variability and provides predictability to monsoonal precipitation, there is also a substantial portion of AAC variability that is independent of ENSO (sometimes called "internal variability"; e.g., Ma et al. 2017; Wang et al. 2018; C.-Y. Wang et al. 2020). There is evidence that the ENSO-independent variability is strong enough that a neutral or even negative state of the AAC (i.e., anomalous cyclone) can be observed in post–El Niño summers. For example, after a strong El Niño event in the winter of 2015/16, the AAC was unexpectedly replaced by an anomalous

---

Corresponding author: Pengcheng Zhang, pczhang@ucsd.edu

DOI: 10.1175/JCLI-D-23-0169.1

cyclone in August; also, in the summer of 2020, a strong AAC caused record flooding in East Asia without a strong preceding El Niño. It has been suggested that the transition in 2016 was related to the summer intraseasonal oscillation (X. Wang et al. 2020), while the IO warming accompanied by downwelling ocean Rossby waves following a record Indian Ocean dipole (IOD) event plays a central role in the 2020 AAC event (Takaya et al. 2020; Zhou et al. 2021). Moreover, Kosaka et al. (2013) and Wang et al. (2018) suggest that ENSO explains less than half of the total sea level pressure variance in the northwestern Pacific, further highlighting the importance of ENSO-independent internal variability.

The leading mode of internal variability in summer is suggested to resemble the ENSO-induced AAC, although it still remains challenging to properly distinguish ENSO-independent variability from ENSO forcing (e.g., Ma et al. 2017; C.-Y. Wang et al. 2018, 2020; X. Wang et al. 2020). The ENSO-independent internal variability includes air–sea coupling modes other than ENSO and atmospheric internal variability. Even in an atmospheric general circulation model without an active ocean, the AAC stands out as a preferred stationary mode of atmospheric variability (Kosaka et al. 2013), with the distinctive spatial structure tapping into barotropic energy conversion of the mean flow (Kosaka and Nakamura 2010; Hu et al. 2019; Wang et al. 2021). With active ocean–atmosphere coupling, the interbasin positive feedback helps the AAC to gain slow time scales beyond a month (Kosaka et al. 2013). Given the difficulties in separating ENSO-independent variability in observations, a realistic representation of internal variability is needed, and more consideration should be given to the dynamical characteristics and implications of the AAC variability in the absence of ENSO forcing.

The present study examines the dynamics of ENSO-independent AAC variability using a novel set of experiments with a coupled atmosphere–ocean climate model. Our simulations build on the tropical Pacific Ocean–Global Atmosphere (POGA) pacemaker simulations first described by Kosaka and Xie (2013). POGA is a useful tool for decomposing ENSO forcing (as the ensemble mean) and internal variability (as the ensemble spread; i.e., deviations from the ensemble mean) (C.-Y. Wang et al. 2020). In an ensemble of POGA simulations, the runs differ only in the initial conditions, but in this setup, the non-ENSO internal variability is likely to be excessively damped due to SST restoring over the tropical Pacific. Here, we remove this artificial damping using a novel experimental setup in which fully coupled simulations are initialized from the POGA pacemaker experiment on 1 January of each year over the 39-yr period of 1983–2021. As shown below, this leads to enhanced AAC variability with month-to-month persistence compared to the original POGA setup. The more realistic representation of internal variability allows a more realistic manifestation of Indo-Pacific cross-basin interactions and AAC variability. Robust precursory signals are identified in the tropical Atlantic, Indian, and northwestern Pacific a season or longer before summer. We clarify the pathway for each precursor to develop into an AAC. The short duration of the available observations is a limiting factor for studying AAC variability, but the 20-member ensemble "hindcast" overcomes this limitation with a 20-time increase in the degrees of freedom in the ensemble spread that represents internal variability.

The remainder of this paper is structured as follows. Section 2 introduces the datasets and model simulations used in the study. Section 3 describes the characteristics of summer AAC variability that is independent of ENSO. Section 4 analyzes three non-ENSO precursory signals that contribute to AAC variability, and in section 5, we discuss how AAC prediction can be improved by including these non-ENSO precursors. We end in section 6 with a summary and discussion.

2. Methods

a. *Model simulations*

We use the tropical Pacific Ocean–Global Atmosphere [POGA; see Kosaka and Xie (2013) for a more detailed description] simulations based on the Geophysical Fluid Dynamics Laboratory coupled model, version 2.1 (CM2.1; Delworth et al. 2006), which provides a realistic representation of the tropical Pacific climate (Wittenberg et al. 2006, 2014). We compare two types of POGA experiments—POGA-pacemaker and POGA-forecast—to evaluate the variability in the Indo-western Pacific region.

In the POGA-pacemaker experiment, SSTs in the tropical Pacific are restored to the daily model climatology plus observed interannual anomaly, while the ocean and atmosphere are coupled and freely running elsewhere. The SST restoring is applied in the top 10 m of the ocean in a region that spans 15°S–15°N, from the American coast to the date line and a triangle wedge extending to 135°E, with a 5° buffer zone in latitude, as shown in Fig. 1a and the brown dashed lines in Fig. 2f. The SST anomalies are derived from Optimum Interpolation SST, version 2.1 (Banzon et al. 2016) from 1982 to 2020. The SST anomalies are defined as deviations from 1982 to 2011 climatology, while the model climatology has been obtained for the same period from a 10-member ensemble of CM2.1 simulations, forced by historical radiative forcing and extended by the representative concentration pathway (RCP) 4.5 scenario. Through an evolving Walker circulation, subsurface conditions in the tropical Pacific adjust to follow the observations.[1] In the POGA-pacemaker experiment, we perform an ensemble of 20 simulations that differ in initial conditions but share the same radiative forcing and tropical Pacific SST. The ensemble mean represents the influence of tropical Pacific SST (predominantly ENSO variability), as the internal variability is assumed to have random phases and amplitudes in different ensemble members and thus be averaged out in the ensemble mean. The ensemble spread is obtained by subtracting the ensemble mean from individual members and represents ENSO-independent internal variability. By design, the ensemble spread in the tropical Pacific is unrealistically suppressed (see the SST response in the restoring region in Fig. 2f), which may damp ocean–atmosphere variability elsewhere through the atmosphere.

---

[1] The correlation between December sea surface height (SSH) in the POGA-pacemaker ensemble mean and in Ocean Reanalysis System 5 (ORAS5) reaches 0.94 ($p < 0.001$) during the period of 1982–2014.

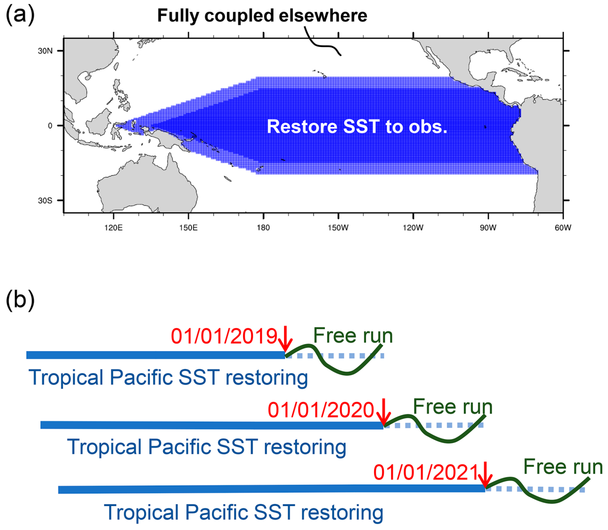

FIG. 1. (a) The SST restoring region (dark blue) and the buffer zone (light blue) in the tropical Pacific for the POGA-pacemaker experiment. (b) A schematic for the POGA-forecast experiment (green curves) that branches from the POGA-pacemaker (blue solid lines). For each ensemble member in the POGA-pacemaker experiment, we obtain 39 segments of 1-yr simulations in the corresponding POGA-forecast experiment.

We perform the POGA-forecast experiment to remove the artificial damping on the tropical Pacific (Fig. 1b). For each ensemble member in the POGA-pacemaker experiment, we restart the model on 1 January and let the model run freely without SST restoring for 1 year. The POGA-initialized ensemble experiment is conducted 39 times to cover the 39-yr period of 1983–2021. For each year, we have 20 ensemble members that share nearly the same ENSO initial conditions but evolve away from each other. Unlike the POGA-pacemaker setup, tropical Pacific SSTs are free to evolve, with the ensemble mean representing the effect of the ocean's initial condition on 1 January. The ensemble spread, which is 20 × 39 years long, represents the internal variability, including that in the tropical Pacific (cf. Figs. 2d,f). Note that there may be ENSO-like SST signals that emerge and evolve spontaneously in the ensemble spread of the POGA-forecast experiment. Since the SST signals are independent of the preceding ENSO and are relatively weak until autumn and winter, we still denote the variability in the ensemble spread as ENSO-independent variability. The comparison of the POGA-forecast and the POGA-pacemaker allows us to study the role of the active tropical Pacific.

All the variables from POGA simulations are interpolated onto a common 1° × 1° grid and the linear trends associated with global warming are removed before further analysis. Following C.-Y. Wang et al. (2020), for better statistical results, all analyses of ensemble spread in this study are based on the 780-yr-long time series concatenated from all ensemble members. To test the robustness of the results, we repeat the same analysis with half of the simulations in POGA experiments and find that the results are qualitatively unchanged.

b. *Observations and reanalysis*

We track ENSO with the oceanic Niño index (ONI; see NOAA 2022b), published by the National Oceanic and Atmospheric Administration's (NOAA) Climate Prediction Center (CPC). The ONI is based on the 3-month running mean of SST anomalies in the Niño-3.4 region (5°N–5°S, 120°–170°W; see NOAA 2022a). NOAA considers El Niño conditions to be present when the ONI is +0.5 or higher, indicating that the east-central tropical Pacific is anomalously warmer than usual, and La Niña conditions to be present when the oceanic Niño index is −0.5 or lower, indicating that the region is cooler than usual (Dahlman 2016; NOAA 2022b). Following these criteria, we use the 3-month average of Niño-3.4 SST anomalies to determine El Niño or La Niña conditions in model simulations.

To benchmark the performance of the POGA simulations, we use wind, precipitation, sea level pressure (SLP), and SST data from the latest European Centre for Medium-Range Weather Forecasts (ECMWF) Reanalysis (ERA5; 0.25° × 0.25° resolution; Hersbach et al. 2020). Monthly anomalies are obtained by subtracting the long-term climatology from the original data, and linear trends are removed before all calculations. To extract the ENSO-independent variability, we use the linear regression model[2] of Wang et al. (2018) to remove variability associated with ONI of the preceding November, December, and January (NDJ; i.e., the peak season of ENSO).

3. Summer coherent mode in NWP

To characterize the AAC mode in the ERA5 reanalysis data and two sets of POGA simulations, we define an AAC index as the first principal component (PC1) of the leading empirical orthogonal function (EOF) of JJA-mean SLP in the NWP region (0°–35°N, 100°–160°E; purple box in Fig. 2a), and the AAC mode is represented as the regressions of SST, SLP, and wind against the AAC index (Fig. 2).

In the raw ERA5 reanalysis, a low-level AAC, centered over the Philippine Sea, is the leading EOF mode and explains 60% of the total variance (Fig. 2a). The anomalous easterlies on the southern flank of the AAC cool the SST by strengthening the background winds east of 140°E and warm the SST by weakening the background winds to the west. These key features, and the SLP, wind, and SST patterns more generally, are well captured in the POGA-forecast and POGA-pacemaker ensemble means (Figs. 2c,e), consistent with Wang et al. (2018). The AAC modes in the POGA-forecast and POGA-pacemaker ensemble means do not show noticeable differences, suggesting that the POGA-forecast experiment does not introduce additional bias in the ENSO-induced AAC mode compared with the POGA-pacemaker experiment.

---

[2] Although the linear relationship may vary on the interdecadal timescale, the running correlation between preceding ENSO and summer AAC remains stable after the 1960s (Wang et al. 2018).

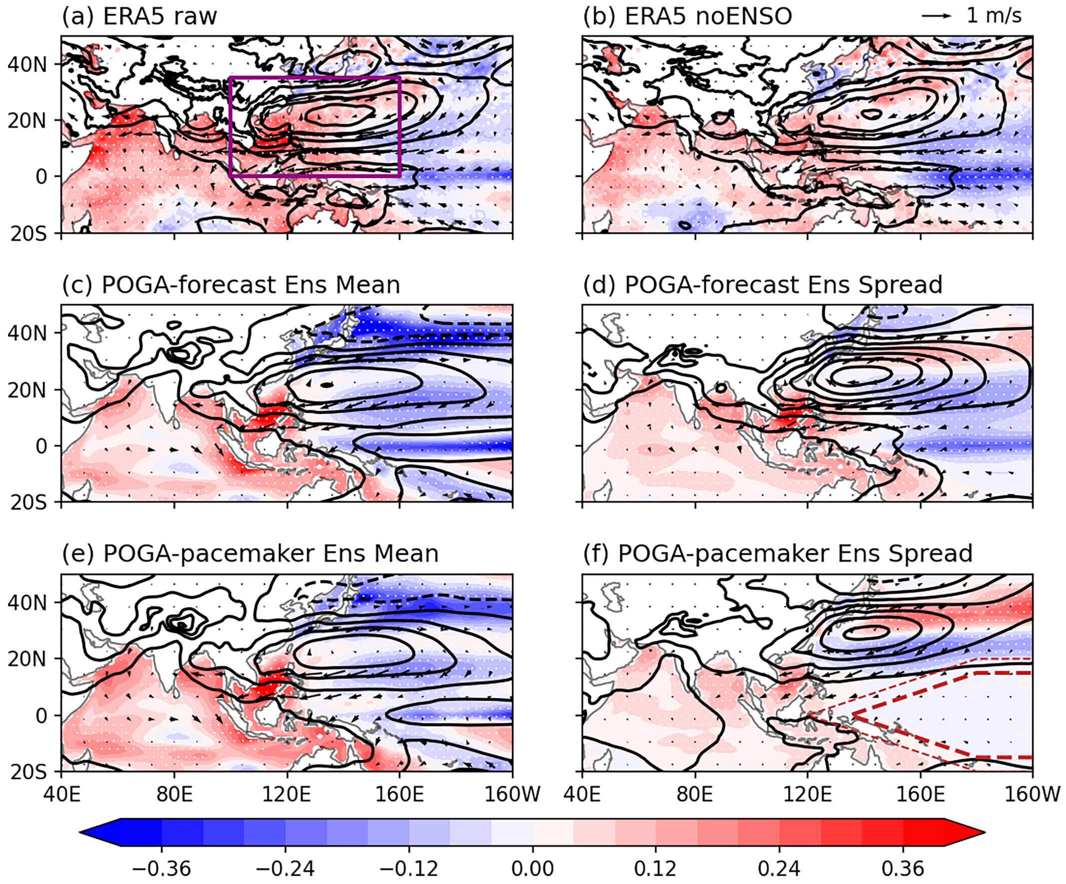

FIG. 2. The structure of the AAC mode shown as JJA SST (shading), SLP (contour), and 10-m wind (arrow) anomalies regressed on the JJA AAC index in (a) ERA5 reanalysis data, (b) ERA5 data with the NDJ ENSO state regressed out, (c) the POGA-forecast ensemble mean, (d) the POGA-forecast ensemble spread, (e) the POGA-pacemaker ensemble mean, and (f) the POGA-pacemaker ensemble spread. The shading interval is 0.04 K, and the contour interval is 0.2 hPa in all panels. Stippling marks the regions where SST regression coefficients are statistically significant at the 95% confidence level, using a Student's *t* test. The purple box in (a) indicates the region in which SLP is used to perform the EOF analysis, and the thick and thin dashed lines in (f) indicate the SST restoring region and buffer zone in the POGA-pacemaker experiment. The leading EOF mode explains 60%, 56%, 83%, 60%, 82%, and 54% of the total variance in (a)–(f), respectively.

a. *Non-ENSO variability*

Following Wang et al. (2018), we estimate the ENSO-independent variability from the ERA5 reanalysis by regressing out the ONI in the preceding NDJ. The resulting leading EOF mode has a similar structure to the leading mode in the original ERA5 reanalysis, although there are minor differences in shape and amplitude (Fig. 2b). Similar AAC modes, including the large-scale atmospheric and oceanic patterns, are captured in the POGA-forecast and POGA-pacemaker ensemble spreads, although the SST responses in the Indian Ocean are relatively weaker because of the absence of preceding El Niño (Figs. 2d,f). As the POGA ensemble spreads represent non-ENSO internal variability, this similarity suggests that AAC variability is an intrinsic mode of the region, rather than a passive response to ENSO forcing. We reconstruct the SLP field using the leading EOF mode only and calculate the variance of SLP averaged in the NWP region, as shown in Table 1. In the POGA experiments, the ENSO-independent AAC variance is 46% and 176% larger than that of the ENSO-induced AAC mode in the POGA-pacemaker and POGA-forecast experiments, respectively, consistent with Kosaka et al. (2013) and Wang et al. (2018; C.-Y. Wang et al. 2020). The high variance explained by the ENSO-unrelated AAC indicates that internal variability plays an important role in the Indo-western Pacific region, although the ratio of internal to ENSO-induced variability may vary on longer time scales. Wang et al. (2018) show that the correlation between preceding ENSO and summer AAC is even lower prior to the 1960s, suggesting a more important role of ENSO-independent variability.

The AAC mode in the POGA-pacemaker ensemble spread (Fig. 2f) is notably biased in the SST restoring region. In the POGA-pacemaker experiment, all the non-ENSO internal variability is strongly suppressed in the SST restoring region. As a result, the AAC mode is substantially biased: SST, SLP, and wind anomalies are damped and displaced to the

TABLE 1. Scaled variance of the leading mode average SLP in POGA-pacemaker and POGA-forecast experiments. The SLP variability is reconstructed by the leading EOF mode and then averaged in the NWP region (purple box in Fig. 2a). All the values are scaled by the variance of the leading mode reconstructed SLP in the POGA-pacemaker ensemble mean.

		EOF1
POGA-pacemaker	Ensemble mean	1
	Ensemble spread	1.46
POGA-forecast	Ensemble mean	0.99
	Ensemble spread	2.74

TABLE 2. Lagged autocorrelation of area-averaged SLP in ensemble spread of POGA-pacemaker and POGA-forecast experiments. The SLP is averaged in the NWP region (purple box in Fig. 2a).

	June–July	July–August
POGA-pacemaker	0.266	0.204
POGA-forecast	0.394	0.397

northwest, constrained by the shape of the restoring region. The SLP variance of the ENSO-independent AAC mode in the NWP region is substantially reduced compared with the POGA-forecast experiment, perhaps due to a lack of interactive feedback in the SST restoring region (Table 1). Table 2 also shows that the summer SLP variability in POGA-pacemaker is much less persistent than in POGA-forecast. A more comprehensive description of the biases in the POGA-pacemaker ensemble spread can be seen in the appendix (cf. Fig. A1 with Fig. 4). Because of these biases, we will focus here on the internal variability as represented by the POGA-forecast ensemble spread, while the ensemble spread of the corresponding POGA-pacemaker runs is only used to investigate the precursory signals before the 1 January initialization.

As the non-ENSO AAC variance exceeds the ENSO-induced one, the correlation between AAC and antecedent ENSO could vary considerably for a limited 39-yr period, depending on the relative strength between ENSO and internal variability. As shown in Fig. 3, the AAC in the ensemble mean is highly correlated with the antecedent ENSO (blue dots), but this connection could become statistically insignificant in individual ensemble members that are only 39 years long (gray dots), especially in the POGA-forecast experiment. The antecedent ENSO is not a bad predictor for summer AAC (the blue dashed line in Fig. 3), but the prediction skill is limited by non-ENSO internal variability. Note that in Fig. 3, the correlation between the AAC index and preceding NDJ ONI is higher in the ensemble mean than in ensemble members except for one statistically insignificant exception in the POGA-forecast, confirming our assumption that the ENSO-independent variability is averaged out in the ensemble mean.

b. Temporal evolution of ENSO-independent AAC

Although the ENSO-independent AAC mode shares a similar structure with the ENSO-induced AAC mode in summer, their temporal evolutions are different. As shown in Fig. 4, the ENSO-independent AAC is not fully established until boreal summer [June–August (JJA); see Fig. 4e], much later than the ENSO-induced AAC (Wang et al. 2003; Xie et al. 2009, 2016; Xie and Zhou 2017). In the preceding winter [December–February (DJF); Fig. 4a] and spring [March–May (MAM); Fig. 4c], only weak easterlies are seen in the tropical NWP. This is because the positive interbasin feedback can only be triggered when the Asian summer monsoon is established and the background mean zonal flow converts to westerly over the TIO. Nonetheless, there exist significant cold SST signals in the NWP, as well as coherent precipitation anomalies as early as in DJF (see the stippling in Figs. 4a,b). We will return to these precursory signals in the next section.

JJA is the peak season of the ENSO-independent AAC mode. Following the onset of background monsoonal westerlies, the easterly wind anomalies on the southern flank of the AAC act to warm the IO SST by reducing evaporative cooling. The warm IO excites the equatorial Kelvin wave, which induces the AAC via low-level Ekman divergence. Accordingly, the monsoon trough divides the regions with opposite SST responses: warm anomalies in the background westerly region west of the monsoon trough and cold anomalies in the background easterly trade wind region. Significant precipitation anomalies are associated with the ENSO-independent AAC mode (Fig. 4f). The colder NWP is accompanied by less precipitation, while the warmer IO is accompanied by more precipitation. However, in the NWP, the dry center is located slightly west of the cold SST center, with the former

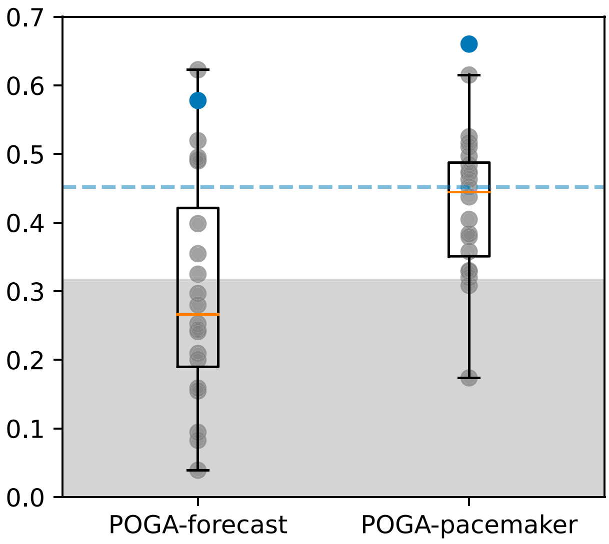

FIG. 3. Correlations between AAC indices and the preceding NDJ Niño-3.4 SST anomaly for POGA-forecast and POGA-pacemaker simulations. The gray points indicate the correlation for each ensemble member, and the box plot shows the quartiles and median. Two blue points represent the correlation between AAC and NDJ Niño-3.4 SST anomaly in the ensemble mean. The gray shading denotes the 95% significance threshold based on the Student's t test. For comparison, the light blue dashed line shows the correlation of AAC in ERA5 with the preceding NDJ ONI.

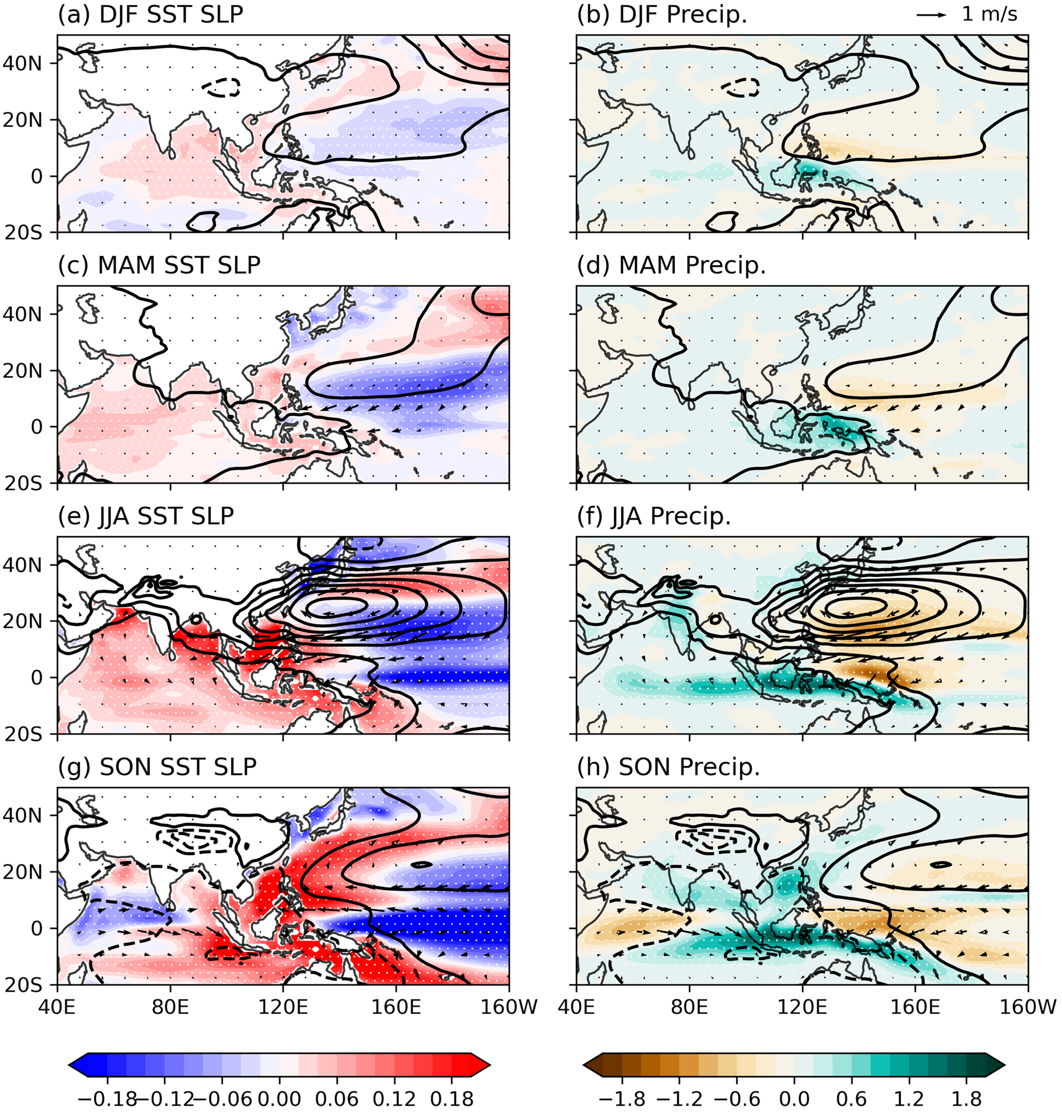

FIG. 4. The seasonal evolution of the ENSO-independent AAC mode shown as (left) SST (shading) and (right) precipitation (shading), along with SLP (contours) and 10-m wind (arrows) anomalies regressed on the JJA AAC index in the POGA-forecast ensemble spread. The shading intervals are 0.02 K for SST and 0.2 mm day^{-1} for precipitation; the contour interval is 0.2 hPa. Stippling marks the regions where regression coefficients are statistically significant at the 95% confidence level, using a Student's *t* test.

south of AAC and the latter southeast of AAC. This mismatch suggests that the precipitation anomalies might be primarily driven by anomalous atmospheric downwelling motion rather than by anomalous oceanic cooling. In the IO, the enhanced precipitation is mainly confined to low latitudes and the precipitation response in NIO is much weaker despite stronger SST warming. Xiang et al. (2013) argued that the "invisible" rainfall response in the NIO is offset by the dry anomalies associated with extended AAC-induced atmospheric downwelling. Over land, precipitation is strengthened in west India, east China, and Japan, indicating that the ENSO-independent AAC modulates the monsoonal rainfall much as the ENSO-induced AAC does.

The AAC persists until autumn [September–November (SON); Fig. 4g] but weakens and is centered slightly eastward. The easterly wind anomalies on the south flank also retreat eastward and have less impact on IO SSTs. In the Pacific, the SST and wind responses exhibit a La Niña–like pattern, with cooling in the central and eastern Pacific and low-level convergence over the Maritime Continent. Further analysis is needed to study the potential interaction between AAC and developing ENSO.

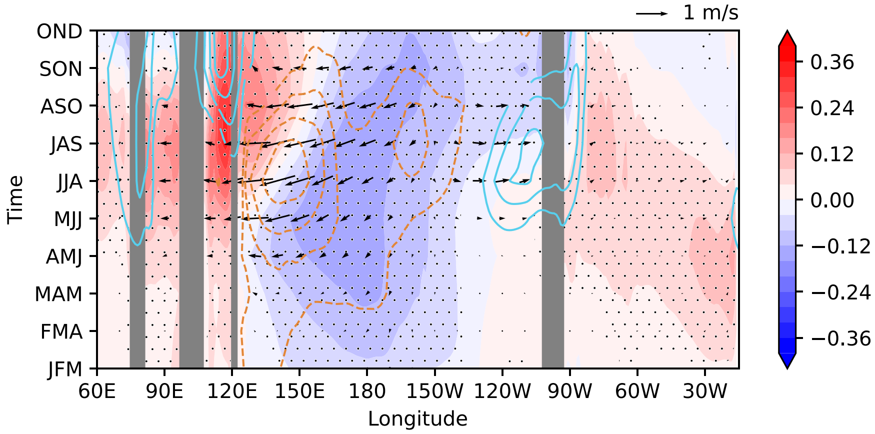

FIG. 5. Seasonal evolution of the ENSO-independent AAC mode shown as the meridional mean SST (shading), precipitation (line contours), and 10-m wind (arrows) anomalies between 10° and 20°N regressed on the JJA AAC index in the POGA-forecast ensemble spread. The shading interval is 0.04 K; the contour interval is 0.2 mm day^{-1}. Stippling marks the regions where SST regression coefficients are statistically significant at the 95% confidence level, using a Student's *t* test. The Arabian Sea, BoB, SCS, Pacific, and Atlantic correspond to the *x* axis from left to right.

4. Non-ENSO precursors

a. Northwestern Pacific SST

Coherent SST and precipitation anomalies emerge in the NWP as early as in the preceding winter (Fig. 4). To further illustrate this precursor signal, we show the evolution of the SST, wind, and precipitation associated with the summer AAC averaged over 10°–20°N in Fig. 5. The southern flank of the AAC lies between 10° and 20°N, so Fig. 5 represents how the easterly wind anomalies induced by the AAC evolve and interact with local SSTs and precipitation. The easterly wind anomalies begin to grow in April–June (AMJ) and reach peak strength in JJA. The easterly wind anomalies cause a cold SST response in the easterly trade wind region and a warm SST response in the westerly monsoon wind region. The division between warm and cold SST responses progresses eastward as the background monsoon westerlies advance eastward, from 120°E in AMJ to 150°E in July–September (JAS).

Notably, the emergence of cold SST anomalies does not rely on anomalous easterly winds. Instead, cold signals in the west and central Pacific appear as early as in January–March (JFM) when no significant atmospheric anomalies exist, consistent with Fig. 4a. This initial cold SST patch gradually strengthens in the spring and intensifies when the AAC is fully established in summer. The precipitation reduction does not follow the development of local SST anomalies but the development of the AAC: the dry anomalies occur later in time and to the west of the SST anomalies. The mismatch in time and longitude suggests that precipitation anomalies in the NWP are not directly driven by local oceanic forcing, although the persistent atmospheric anomalies must be anchored by SST.

The NWP cool patch contributes to the AAC mode by multiple pathways. The negative SST anomalies can induce local precipitation responses and further intensify the AAC via atmospheric Rossby waves (e.g., Wang et al. 2003). We indeed observe dry anomalies associated with cold SST anomalies (the brown contours in Fig. 5), although the dry center does not exactly match the cold center in space. The cold anomalies could enhance the precipitation over nearby warm anomalies, as we observe enhanced precipitation in the IO and Maritime Continent in spring (Fig. 4), which is consistent with Wang et al. (2013), who emphasize this cold–warm dipole pattern. Moreover, the advection of reduced moist enthalpy associated with the SST cooling has also been argued to contribute to the AAC (Wu et al. 2017; Wang et al. 2022). These factors combine to support the AAC mode in the absence of ENSO forcing.

b. Tropical North Atlantic SST

The second non-ENSO precursor lies in the tropical North Atlantic (TNA) Ocean, where preceding warm SST anomalies are found (Fig. 5). The anomalously warm TNA SST emerges as early as in February–April (FMA) and peaks in AMJ, roughly one season before the summer AAC. In AMJ, the warming is stronger in the east TNA than in the west TNA. As the AAC strengthens, the warm SSTs are confined to the western TNA during summer. These preceding SST anomalies suggest a potential precursor at least one season ahead of the summer AAC (e.g., in MAM).

To explore how this springtime TNA warming influences the ensuing summer AAC variability, the responses of SST, SLP, 10-m wind, and precipitation to spring TNA SST anomalies are shown in Fig. 6. Like the cool patch in NWP, the warm patch in TNA emerges in the preceding winter. Strong SLP anomalies are found in the northern Atlantic and northeast Pacific. Easterly wind anomalies in response to TNA warming in the IO strengthen the background mean wind and cool the IO SST, while the westerly wind and warm SST

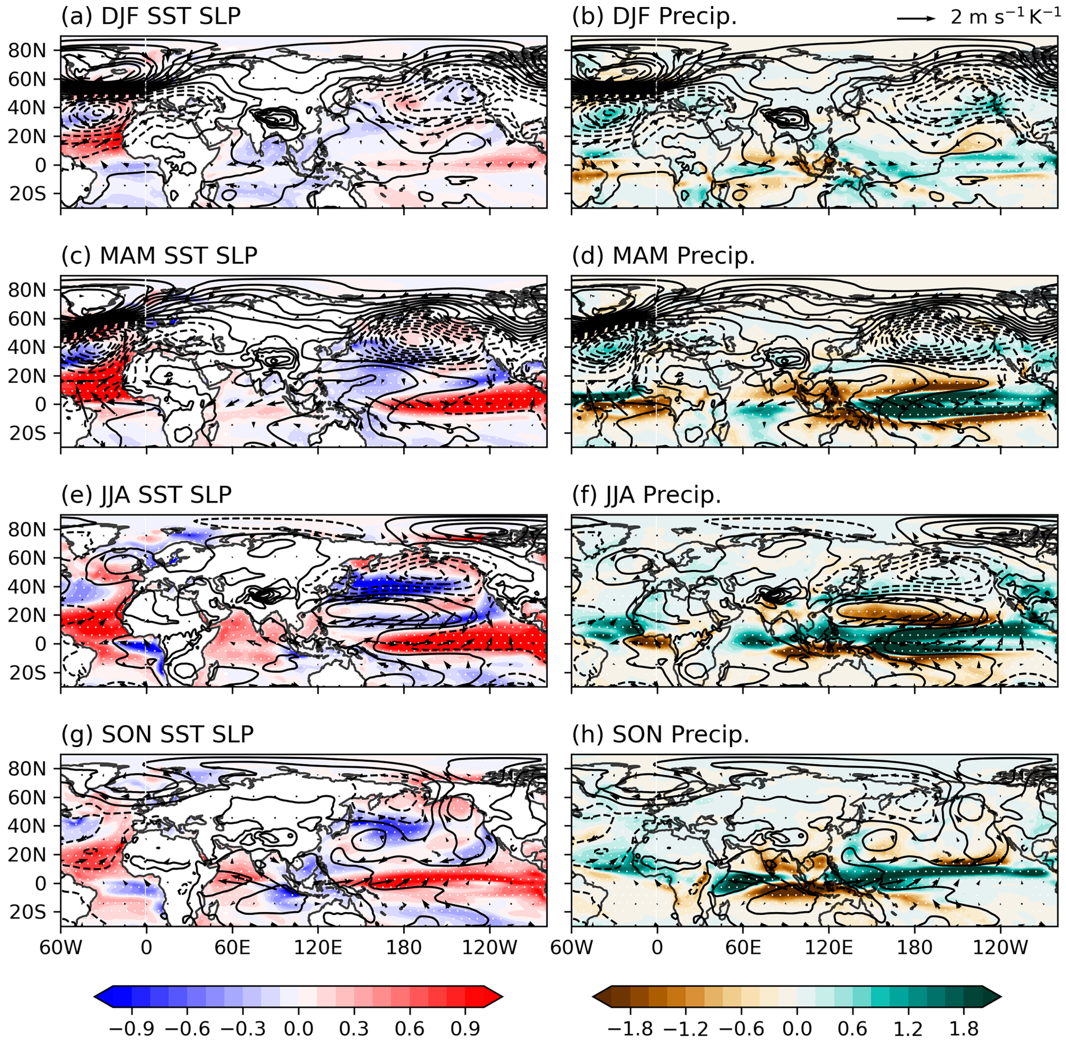

FIG. 6. Seasonal evolution of (left) SST (shading) and (right) precipitation (shading) along with SLP (contours) and 10-m wind (arrows) anomalies regressed on MAM TNA SST anomalies in the POGA-forecast ensemble spread. The TNA SST anomalies are averaged over 0°–20°N, 22°–83°W. The shading intervals are 0.1 K K^{-1} for SST and 0.2 mm day^{-1} K^{-1} for precipitation; the contour interval is 0.5 hPa K^{-1}. Stippling marks the regions where regression coefficients for those shown by shading are statistically significant at the 95% confidence level, using a Student's *t* test.

anomalies in the equatorial Pacific suggest possible Bjerknes feedback. In spring, the warm signals in TNA and the eastern equatorial Pacific continue to intensify. Meanwhile, as the background wind reverses, the easterly wind anomalies start to warm the tropical IO (Figs. 6c,d). This IO warming further strengthens and expands to a larger area in summer as the background monsoonal wind is established, and the warming signals extend to all tropical ocean basins. Warm SSTs in equatorial oceans strengthen tropical ascending motions, as indicated by the enhanced precipitation along the equator (Fig. 6f). This causes the atmospheric subsidence in the subtropics to strengthen. As a result, positive SLP anomalies appear in the subtropical Pacific and contribute to the summer AAC (Figs. 6e,f), although this high pressure band is more zonally extensive than the AAC in Fig. 2.

The above results indicate that the precursory effects of the TNA on the NWP AAC do not necessarily rely on preceding ENSO events, as there is no initial ENSO signal in the POGA ensemble spread by design. Nevertheless, the warm SST anomalies after spring in the eastern equatorial Pacific resemble an El Niño event (Figs. 6c,e). This El Niño–like warming does not match the large-scale SST pattern in the AAC mode (see Figs. 2 and 4). Previous studies, although under different contexts and using different setups, show that TNA warming can induce an AAC without substantial tropical Pacific warming (e.g., Li et al. 2016; L. Chen et al. 2022; W. Chen et al. 2022). To reconcile these results, we repeat the analysis with the POGA-pacemaker experiment. The Atlantic precursor is still well recognized without tropical Pacific SST response being allowed (not shown). Hence, the impact of warm TNA

SST on AAC does not necessarily rely on the mediation of tropical Pacific SST, although the El Niño–like warming in Figs. 6c and 6e may contribute to the AAC.

c. *Indian Ocean Rossby wave*

In the theory of the IPOC, the basinwide IO warming that facilitates AAC persistence is viewed as forced by preceding El Niños through the atmospheric bridge (Alexander et al. 2002), but not all IO warming events are fully driven by El Niño. Ding et al. (2022) suggest that the Indian Ocean basin mode is intrinsic to the IO even without interaction with other basins. We indeed observe ENSO-independent basinwide IO warming in the preceding winter and spring (Figs. 4a,c). Inspired by the strong AAC event in 2020 summer that has been traced back to the extreme IOD event in 2019 (Takaya et al. 2020; Zhou et al. 2021), we search for a precursor in the Indian Ocean.

IO warming can be induced by downwelling oceanic waves independent of ENSO (e.g., triggered by IOD rather than by El Niño; Ding et al. 2022; Liu et al. 2022). Xie et al. (2002) point out the important role of the slow propagating oceanic Rossby wave in the tropical southwest Indian Ocean (SWIO). Du et al. (2009) and Xie et al. (2016) confirm that the warming associated with downwelling oceanic Rossby waves is a key component of the IPOC. Chen et al. (2021) show that in a global coupled model, imposing a warming signal in SWIO triggers the positive interbasin feedback and drives an AAC-like response in the NWP, as happened in summer 2020.

To evaluate the potential connection between Indian Ocean Rossby waves and the AAC, we perform a maximum covariance analysis between SON sea surface height (SSH) in the IO and the subsequent JJA SLP in the NWP. As shown in Fig. 7, the leading mode exhibits a pair of downwelling oceanic Rossby waves in the tropical IO on either side of the equator, indicated by the positive SSH anomalies. The positive SSH anomalies are stronger south than north of the equator because of asymmetric wind forcing (Xie et al. 2002). The equatorial Kelvin wave turns at Sumatra and the Indo-China Peninsula into a coastal Kelvin wave in the east IO and BoB. Note that we choose the IO SSH in SON because the IOD is an important forcing of oceanic waves and peaks in autumn. Repeating the analysis with IO SSH data in a different season, we would see slow propagation of oceanic Rossby waves that anchors the SWIO warming, which can also be seen in the Hovmöller diagram of Indian Ocean SSH regressed onto the JJA AAC index (Fig. 8). An atmospheric AAC appears in the NWP in the summer of the subsequent year, with the same structure as in Figs. 2 and 3. This leading mode explains 40.2% of the total covariance, suggesting a physical connection between oceanic waves in the IO and the AAC in NWP.

5. Implications for predictability

To illustrate how these precursors can help predict the ENSO-independent AAC mode, we calculate the lagged correlation between the JJA-mean AAC index and three precursory signals: NWP SST, TNA SST, and SWIO SSH, as shown in Fig. 9. All three precursors are significantly correlated with the summer AAC index at least 1 month ahead of summer. The strongest correlations are seen with the NWP SST, for which the correlation becomes statistically significant as early as OND of the preceding year. This suggests that the local SST feedback is always active in the trade wind region. The TNA SST is also significantly correlated with the AAC, although the predictability is lower than NWP SST. The temporal evolution of the NWP and TNA correlations are consistent with the discussion in section 4, with the former originating earlier than the latter. For the SWIO SSH, the correlation is significant, albeit marginally.

(a) SON SSH

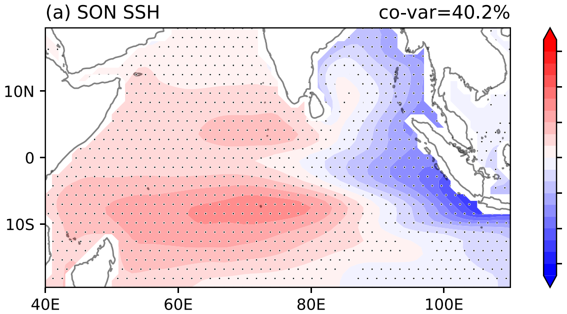

(b) JJA SLP

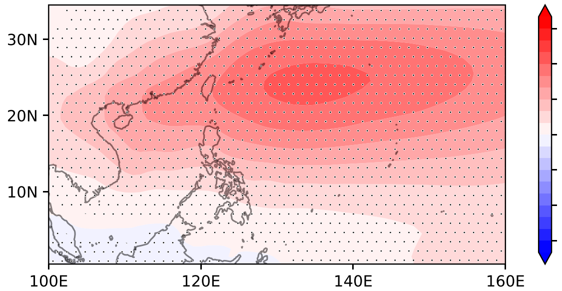

FIG. 7. Leading mode for maximum covariance analysis of (a) SON SSH in the TIO and (b) JJA SLP in the NWP, indicated by regressions on respective expansion coefficients. The leading mode explains 40.2% of the total covariance, and the correlation between two expansion coefficients is 0.133 ($p < 0.01$). The shading interval is 1 cm for SSH and 0.2 hPa for SLP. Stippling marks the regions where regression coefficients are statistically significant at the 95% confidence level, using a Student's *t* test.

The above results suggest that by considering non-ENSO precursors, one can improve AAC predictive skill compared to prediction schemes based solely on ENSO. To test this hypothesis, we use ERA5 data and a 500-yr preindustrial control simulation with the Community Earth System Model version 2 (CESM2). CESM2 can represent AAC variability with reasonable temporal and spatial structure (not shown).[3] In both the reanalysis and model simulation, we hindcast (or reconstruct) the AAC index based on ENSO only and multivariate linear regression using the non-ENSO precursors identified in the previous section. As shown in Fig. 10, incorporating other precursory

---

[3] Wang et al. (2023) confirmed it using an earlier version of CESM.

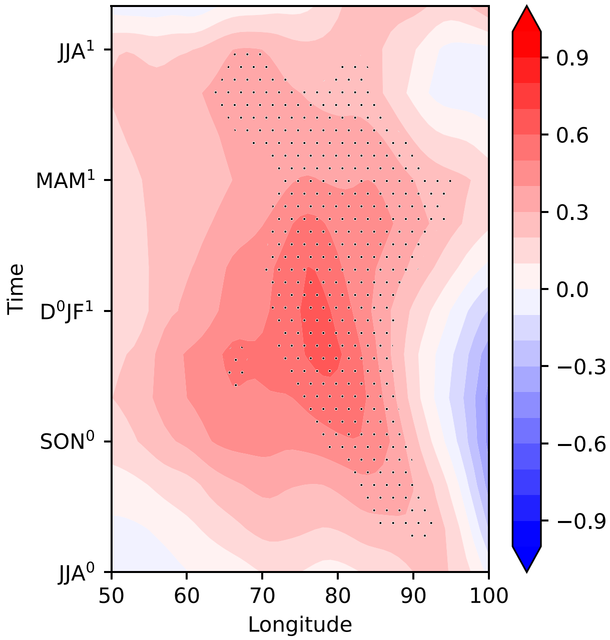

FIG. 8. Seasonal evolution of precursory Indian Ocean SSH anomalies averaged between 5° and 10°S shown as regression on JJA AAC index in the POGA-forecast ensemble spread. The shading interval is 0.1 cm. Stippling marks the regions where regression coefficients are statistically significant at the 95% confidence level, using a Student's *t* test. The "0" and "1" superscripts indicate the year preceding and concurrent with the JJA season of the AAC index, respectively.

signals significantly increases the predictability compared to using ENSO on its own, as indicated by the correlation between the AAC index obtained from EOF analysis and the reconstruction based on multivariate linear regression. When considering all three non-ENSO precursors as well as the preceding ENSO, the correlation reaches ~0.7 in both the ERA5 data and the CESM simulation, much higher than the correlation between the AAC and the preceding ENSO alone, and more AAC variance can be explained in the multivariate regression model. Note that in the case of ERA5, the contributions of the SWIO and NWP precursors are marginal, consistent with Lu et al. (2023), possibly because the ERA5 record is too short to sample the full sensitivity to non-ENSO internal variability. Indeed, in the long CESM2 simulation, non-ENSO contributions are larger and more equal from the three internal precursors.

6. Summary

In this study, we have conducted an ensemble of POGA-initialized forecasts and shown that it represents ENSO-independent variability more realistically than the original POGA-pacemaker simulation. The leading mode of atmospheric variability over the northwest Pacific exhibits an anomalous anticyclone centered over the Philippine Sea while the easterly wind anomalies on the south flank extend as far as to the Arabian Sea. The AAC structure is similar regardless of whether it is forced by ENSO or not, supporting the notion that the AAC is an intrinsic mode of the summer monsoon (Xie 2022, 292–293), energized by barotropic energy conversion from the confluence of the background monsoon westerlies over the northern IO and the South China Sea and easterly trade winds to the east (Kosaka and Nakamura 2010; Hu et al. 2019; Wang et al. 2021). The AAC is further amplified by and gains month-to-month persistence from coupled ocean–atmospheric feedbacks: the easterly wind anomalies on the south flank of the AAC decelerate the monsoon westerlies and warm the Indian Ocean by reducing surface evaporation, while the warmed Indian Ocean helps sustain the AAC by exciting an atmospheric equatorial Kelvin wave. This indicates that the interbasin positive feedback is a key element of the IPOC mode, although El Niño events often trigger the coupled mode.

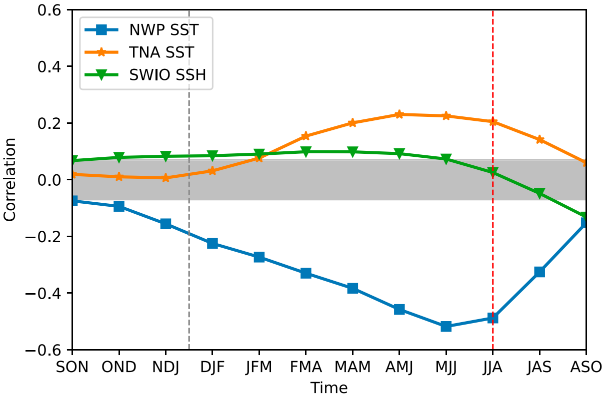

FIG. 9. Lagged correlation between the JJA AAC index and three precursors in the ensemble spread of POGA-forecast simulations: NWP SST anomalies averaged over 5°–20°N, 140°E–180°; TNA SST anomalies averaged over 0°–20°N, 22°–83°W; and SWIO SSH anomalies averaged over 5°–10°S, 60°–80°E. The red dashed line indicates lag 0; to the left of the red dashed lines means the precursor leads AAC. The gray dashed line divides the concurrent year and the preceding year. The gray shading denotes the 95% significance threshold based on Student's *t* test.

The strong AAC event in 2020 summer shows that ENSO is often, but not always, the major driver of IPOC. Using the large-ensemble POGA forecast, we have identified three robust non-ENSO precursors in three tropical ocean basins for AAC variability: the preseason SST cooling in NWP, TNA SST warming in spring, and downwelling oceanic Rossby waves in the SWIO. Without a strong preceding El Niño, a retrospective analysis showed that the 2020 AAC event was predicted by operational dynamical models—but not by empirical forecasts—because of the slow propagation of SWIO downwelling Rossby waves (Takaya et al. 2020; Zhou et al. 2021). Properly initialized, realistic dynamical models can in principle make skillful predictions even though the precursor of SWIO downwelling Rossby waves has not been previously identified from limited observations. Reflection on the 2020 AAC forecast has led to changes in weighing dynamical and empirical forecasts (Lu and Takaya 2021).

Our tests with ERA5 observations and a long CESM2 simulation confirm that incorporating non-ENSO precursors

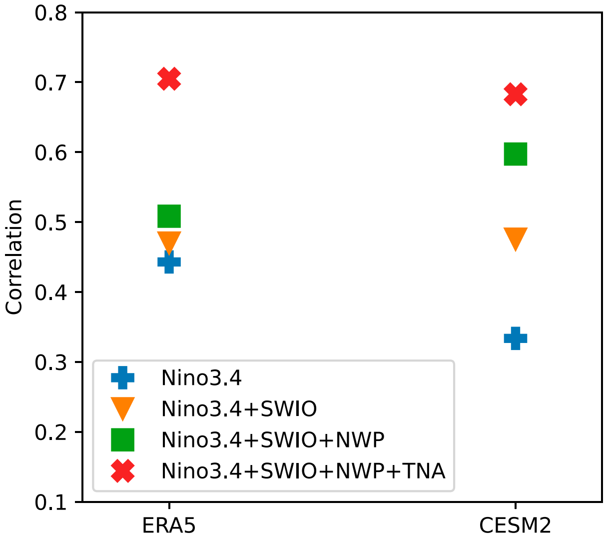

FIG. 10. Contributions of four predictors in ERA5 and long CESM2 simulations, shown as correlations between raw AAC variability and four reconstructions that include one additional predictor in the linear regression model at a time: antecedent NDJ Niño-3.4 SST (blue markers), SON SWIO SSH (orange), MAM NWP SST (green), and MAM TNA SST (red). The correlation increases are statistically significant at the 95% confidence level, using a Monte Carlo significance test.

markedly increases AAC predictability. Although the contribution from individual precursors may vary depending on non-ENSO internal variability, the new prediction method represents an important step forward from traditional ENSO-based AAC prediction.

Our list of non-ENSO precursory signals for AAC variability is by no means exhaustive. For example, there are extratropical signals in the North Pacific in Fig. 4c, but how extratropical signals influence the tropical AAC mode remains to be clarified. X. Chen et al. (2022) suggest that Arctic sea ice loss was a contributor to the 2020 summer extreme event, while atmospheric internal variability, including the intraseasonal oscillation (X. Wang et al. 2020), Silk Road pattern (Li et al. 2017), and quasi-biennial oscillation in the stratosphere (Huangfu et al. 2022), could potentially modulate the monsoonal circulation in the NWP. Further research on how these factors modulate the IPOC mode is needed.

Acknowledgments. The manuscript was much improved by constructive comments and feedback from three anonymous reviewers. We thank Matt Luongo and Ben Taylor for their helpful comments on earlier versions of this manuscript. This work was supported by the National Science Foundation (AGS 2105654). Y. K. was supported by the Japanese Ministry of Education, Culture, Sports, Science and Technology (JPMXD0722680395), by the Japan Society for the Promotion of Science (19H05703, JP22H01302, JP23H01241, and JP23H01250), and by the Environment Research and Technology Development Fund (JPMEERF20222002) of the Environmental Restoration and Conservation Agency provided by the Ministry of the Environment of Japan.

Data availability statement. The ERA5 data are available at the Copernicus Climate Data Store (https://doi.org/10.24381/cds.6860a573). The ONI index is available on the CPC website (https://origin.cpc.ncep.noaa.gov/products/analysis_monitoring/ensostuff/ONI_v5.php). The POGA simulation data are available from the corresponding author upon reasonable request.

APPENDIX

Temporal Evolution of ENSO-Independent AAC in the POGA-Pacemaker Experiment

For comparison, we show the evolution of ENSO-independent AAC mode as in Fig. 4 but for the POGA-pacemaker experiment (Fig. A1), in which no SST spread is allowed by design in the restoring region (see Fig. 1 and the dashed lines Fig. 2f). Similar to Fig. 4, the ENSO-independent AAC in Fig. A1 is not fully established until JJA, but precursory cold SST signals in the NWP can still be seen in the preceding winter and spring. However, the position of the cold anomalies is constrained by the SST restoring region indicated by the sharp edge of the cool patch. Meanwhile, we do not observe strong precipitation signals in subtropics (Figs. A1b,d). The ENSO-independent AAC mode peaks in JJA as in Fig. 4 but is displaced to the northwest of the restoring region, coordinated with the SST anomalies (Fig. A1e). The tropical precipitation and wind anomalies are also strongly damped due to reduced tropical SST variability (Fig. A1f). In the following autumn, the pressure anomalies almost disappear in the NWP and the SST anomalies in the NWP and IO weaken as well (Figs. A1g,h). The weakened persistence of the AAC highlights the importance of active coupling in the tropical Pacific.

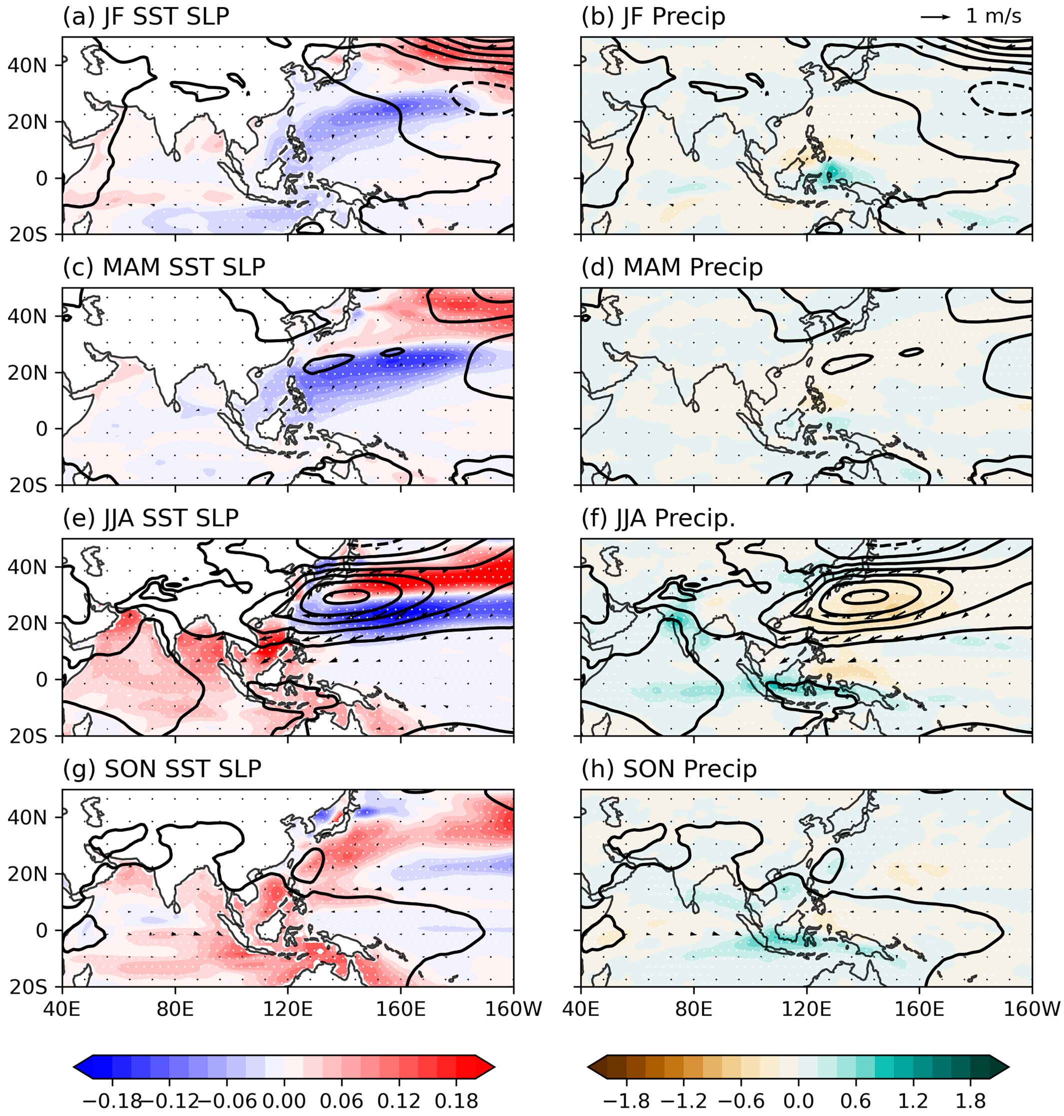

FIG. A1. As in Fig. 4, but for the POGA-pacemaker ensemble spread.

REFERENCES

Alexander, M. A., I. Bladé, M. Newman, J. R. Lanzante, N.-C. Lau, and J. D. Scott, 2002: The atmospheric bridge: The influence of ENSO teleconnections on air–sea interaction over the global oceans. *J. Climate*, **15**, 2205–2231, https://doi.org/10.1175/1520-0442(2002)015<2205:TABTIO>2.0.CO;2.

Banzon, V., T. M. Smith, T. M. Chin, C. Liu, and W. Hankins, 2016: A long-term record of blended satellite and in situ sea-surface temperature for climate monitoring, modeling and environmental studies. *Earth Syst. Sci. Data*, **8**, 165–176, https://doi.org/10.5194/essd-8-165-2016.

Chen, L., G. Li, B. Lu, Y. Li, C. Gao, S.-M. Long, X. Li, and Z. Wang, 2022: Two approaches of the spring North Atlantic sea surface temperature affecting the following July precipitation over central China: The tropical and extratropical pathways. *J. Climate*, **35**, 2969–2986, https://doi.org/10.1175/JCLI-D-21-1012.1.

Chen, W., R. Lu, and H. Ding, 2022: A decadal intensification in the modulation of spring western tropical Atlantic sea surface temperature to the following winter ENSO after the mid-1980s. *Climate Dyn.*, **59**, 3643–3655, https://doi.org/10.1007/s00382-022-06288-z.

Chen, X., Z. Wen, Y. Song, and Y. Guo, 2022: Causes of extreme 2020 Meiyu-Baiu rainfall: A study of combined effect of Indian Ocean and Arctic. *Climate Dyn.*, **59**, 3485–3501, https://doi.org/10.1007/s00382-022-06279-0.

Chen, Z., Z. Li, Y. Du, Z. Wen, R. Wu, and S.-P. Xie, 2021: Trans-basin influence of southwest tropical Indian Ocean warming during early boreal summer. *J. Climate*, **34**, 9679–9691, https://doi.org/10.1175/JCLI-D-20-0925.1.

Dahlman, L., 2016: Climate variability: Oceanic Niño Index. Accessed September 2022, https://www.climate.gov/news-features/understanding-climate/climate-variability-oceanic-nino-index.

Delworth, T. L., and Coauthors, 2006: GFDL's CM2 global coupled climate models. Part I: Formulation and simulation characteristics. *J. Climate*, **19**, 643–674, https://doi.org/10.1175/JCLI3629.1.

Ding, R., I.-S. Kang, R. Farneti, F. Kucharski, F. D. Sante, J. Xuan, F. Zhou, and T. Zhang, 2022: The internal and ENSO-forced modes of the Indian Ocean sea surface temperature. *J. Climate*, **35**, 4191–4206, https://doi.org/10.1175/JCLI-D-21-0403.1.

Du, Y., S.-P. Xie, G. Huang, and K. Hu, 2009: Role of air–sea interaction in the long persistence of El Niño–induced North Indian Ocean warming. *J. Climate*, **22**, 2023–2038, https://doi.org/10.1175/2008JCLI2590.1.

Hersbach, H., and Coauthors, 2020: The ERA5 global reanalysis. *Quart. J. Roy. Meteor. Soc.*, **146**, 1999–2049, https://doi.org/10.1002/qj.3803.

Hu, K., G. Huang, S.-P. Xie, and S.-M. Long, 2019: Effect of the mean flow on the anomalous anticyclone over the Indo-northwest Pacific in post-El Niño summers. *Climate Dyn.*, **53**, 5725–5741, https://doi.org/10.1007/s00382-019-04893-z.

Huangfu, J., Y. Tang, L. Wang, W. Chen, R. Huang, and T. Ma, 2022: Joint influence of the quasi-biennial oscillation and Indian Ocean basin mode on tropical cyclone occurrence frequency over the western North Pacific. *Climate Dyn.*, **59**, 3439–3449, https://doi.org/10.1007/s00382-022-06276-3.

Kosaka, Y., and H. Nakamura, 2010: Mechanisms of meridional teleconnection observed between a summer monsoon system and a subtropical anticyclone. Part I: The Pacific–Japan pattern. *J. Climate*, **23**, 5085–5108, https://doi.org/10.1175/2010JCLI3413.1.

——, and S.-P. Xie, 2013: Recent global-warming hiatus tied to equatorial Pacific surface cooling. *Nature*, **501**, 403–407, https://doi.org/10.1038/nature12534.

——, ——, N.-C. Lau, and G. A. Vecchi, 2013: Origin of seasonal predictability for summer climate over the northwestern Pacific. *Proc. Natl. Acad. Sci. USA*, **110**, 7574–7579, https://doi.org/10.1073/pnas.1215582110.

Li, C., W. Chen, X. Hong, and R. Lu, 2017: Why was the strengthening of rainfall in summer over the Yangtze River valley in 2016 less pronounced than that in 1998 under similar preceding El Niño events?—Role of midlatitude circulation in August. *Adv. Atmos. Sci.*, **34**, 1290–1300, https://doi.org/10.1007/s00376-017-7003-8.

Li, S., J. Lu, G. Huang, and K. Hu, 2008: Tropical Indian Ocean basin warming and East Asian summer monsoon: A multiple AGCM study. *J. Climate*, **21**, 6080–6088, https://doi.org/10.1175/2008JCLI2433.1.

Li, X., S.-P. Xie, S. T. Gille, and C. Yoo, 2016: Atlantic-induced pan-tropical climate change over the past three decades. *Nat. Climate Change*, **6**, 275–279, https://doi.org/10.1038/nclimate2840.

Liu, M., M. J. McPhaden, H.-L. Ren, M. A. Balmaseda, and R. Wang, 2022: Oceanic heat content as a predictor of the Indian Ocean dipole. *J. Geophys. Res. Oceans*, **127**, e2022JC018896, https://doi.org/10.1029/2022JC018896.

Lu, B., and Y. Takaya, 2021: Record Meiyu-Baiu of 2020: Reflections for prediction. *Sci. Bull.*, **66**, 1939–1941, https://doi.org/10.1016/j.scib.2021.05.011.

Lu, T., Z. Zhu, Y. Yang, J. Ma, and G. Huang, 2023: Formation mechanism of the ENSO-independent summer western North Pacific anomalous anticyclone. *J. Climate*, **36**, 1711–1726, https://doi.org/10.1175/JCLI-D-22-0271.1.

Ma, J., S.-P. Xie, and H. Xu, 2017: Intermember variability of the summer northwest Pacific subtropical anticyclone in the ensemble forecast. *J. Climate*, **30**, 3927–3941, https://doi.org/10.1175/JCLI-D-16-0638.1.

Masumoto, Y., and G. Meyers, 1998: Forced Rossby waves in the southern tropical Indian Ocean. *J. Geophys. Res.*, **103**, 27 589–27 602, https://doi.org/10.1029/98JC02546.

NOAA, 2022a: Climate Prediction Center—Four El Niño regions. Accessed September 2022, https://www.cpc.ncep.noaa.gov/products/analysis_monitoring/ensostuff/nino_regions.shtml.

——, 2022b: Cold and warm episodes by season. Accessed October 2022, https://origin.cpc.ncep.noaa.gov/products/analysis_monitoring/ensostuff/ONI_v5.php.

Takaya, Y., I. Ishikawa, C. Kobayashi, H. Endo, and T. Ose, 2020: Enhanced Meiyu-Baiu rainfall in early summer 2020: Aftermath of the 2019 super IOD event. *Geophys. Res. Lett.*, **47**, e2020GL090671, https://doi.org/10.1029/2020GL090671.

Terao, T., and T. Kubota, 2005: East-west SST contrast over the tropical oceans and the post El Niño western North Pacific summer monsoon. *Geophys. Res. Lett.*, **32**, L15706, https://doi.org/10.1029/2005GL023010.

Wang, B., R. Wu, and T. Li, 2003: Atmosphere–warm ocean interaction and its impacts on Asian–Australian monsoon variation. *J. Climate*, **16**, 1195–1211, https://doi.org/10.1175/1520-0442(2003)16<1195:AOIAII>2.0.CO;2.

——, B. Xiang, and J.-Y. Lee, 2013: Subtropical high predictability establishes a promising way for monsoon and tropical storm predictions. *Proc. Natl. Acad. Sci. USA*, **110**, 2718–2722, https://doi.org/10.1073/pnas.1214626110.

Wang, C.-Y., S.-P. Xie, and Y. Kosaka, 2018: Indo-western Pacific climate variability: ENSO forcing and internal dynamics in a tropical Pacific pacemaker simulation. *J. Climate*, **31**, 10 123–10 139, https://doi.org/10.1175/JCLI-D-18-0203.1.

——, ——, and ——, 2020: ENSO-unrelated variability in Indo–northwest Pacific climate: Regional coupled ocean–atmospheric feedback. *J. Climate*, **33**, 4095–4108, https://doi.org/10.1175/JCLI-D-19-0426.1.

——, X.-T. Zheng, and S.-P. Xie, 2023: Enhanced ENSO-unrelated summer variability in the Indo–western Pacific under global warming. *J. Climate*, **36**, 1749–1765, https://doi.org/10.1175/JCLI-D-22-0450.1.

Wang, X., S.-P. Xie, and Z. Guan, 2020: Atmospheric internal variability in the summer Indo–northwestern Pacific: Role of the intraseasonal oscillation. *J. Climate*, **33**, 3395–3410, https://doi.org/10.1175/JCLI-D-19-0794.1.

——, ——, ——, and M. Wang, 2021: A common base mode of Asian summer monsoon variability across timescales. *J. Climate*, **34**, 7359–7371, https://doi.org/10.1175/JCLI-D-20-0856.1.

Wang, Y., B. Wu, and T. Zhou, 2022: Maintenance of western North Pacific anomalous anticyclone in boreal summer by wind-induced moist enthalpy advection mechanism. *J. Climate*, **35**, 4499–4511, https://doi.org/10.1175/JCLI-D-21-0708.1.

Wittenberg, A. T., A. Rosati, N.-C. Lau, and J. J. Ploshay, 2006: GFDL's CM2 global coupled climate models. Part III: Tropical Pacific climate and ENSO. *J. Climate*, **19**, 698–722, https://doi.org/10.1175/JCLI3631.1.

——, ——, T. L. Delworth, G. A. Vecchi, and F. Zeng, 2014: ENSO modulation: Is it decadally predictable? *J. Climate*, **27**, 2667–2681, https://doi.org/10.1175/JCLI-D-13-00577.1.

Wu, B., T. Li, and T. Zhou, 2010: Relative contributions of the Indian Ocean and local SST anomalies to the maintenance of the western North Pacific anomalous anticyclone during the El Niño decaying summer. *J. Climate*, **23**, 2974–2986, https://doi.org/10.1175/2010JCLI3300.1.

——, T. Zhou, and T. Li, 2017: Atmospheric dynamic and thermodynamic processes driving the western North Pacific anomalous anticyclone during El Niño. Part I: Maintenance mechanisms. *J. Climate*, **30**, 9621–9635, https://doi.org/10.1175/JCLI-D-16-0489.1.

Xiang, B., B. Wang, W. Yu, and S. Xu, 2013: How can anomalous western North Pacific subtropical high intensify in late summer? *Geophys. Res. Lett.*, **40**, 2349–2354, https://doi.org/10.1002/grl.50431.

Xie, S.-P., 2022: *Coupled Atmosphere–Ocean Dynamics: From El Niño to Climate Change*. 1st ed. Elsevier, 432 pp.

——, and Z.-Q. Zhou, 2017: Seasonal modulations of El Niño–related atmospheric variability: Indo–western Pacific Ocean feedback. *J. Climate*, **30**, 3461–3472, https://doi.org/10.1175/JCLI-D-16-0713.1.

——, H. Annamalai, F. A. Schott, and J. P. McCreary Jr., 2002: Structure and mechanisms of south Indian Ocean climate variability. *J. Climate*, **15**, 864–878, https://doi.org/10.1175/1520-0442(2002)015<0864:SAMOSI>2.0.CO;2.

——, K. Hu, J. Hafner, H. Tokinaga, Y. Du, G. Huang, and T. Sampe, 2009: Indian Ocean capacitor effect on Indo–western Pacific climate during the summer following El Niño. *J. Climate*, **22**, 730–747, https://doi.org/10.1175/2008JCLI2544.1.

——, Y. Kosaka, Y. Du, K. Hu, J. S. Chowdary, and G. Huang, 2016: Indo-western Pacific Ocean capacitor and coherent climate anomalies in post-ENSO summer: A review. *Adv. Atmos. Sci.*, **33**, 411–432, https://doi.org/10.1007/s00376-015-5192-6.

Yang, J., Q. Liu, S.-P. Xie, Z. Liu, and L. Wu, 2007: Impact of the Indian Ocean SST basin mode on the Asian summer monsoon. *Geophys. Res. Lett.*, **34**, L02708, https://doi.org/10.1029/2006GL028571.

Zhou, Z.-Q., S.-P. Xie, and R. Zhang, 2021: Historic Yangtze flooding of 2020 tied to extreme Indian Ocean conditions. *Proc. Natl. Acad. Sci. USA*, **118**, e2022255118, https://doi.org/10.1073/pnas.2022255118.

Zhu, J., Y. Yu, Z. Guan, and X. Wang, 2022: Dominant coupling mode of SST in maritime continental region and East Asian summer monsoon circulation. *J. Geophys. Res. Atmos.*, **127**, e2022JD036739, https://doi.org/10.1029/2022JD036739.